Chemical Engineering Science 179 (2018) 133–149

Contents lists available at ScienceDirect

Chemical Engineering Science

journal homepage: www.elsevier.com/locate/ces

Computational fluid dynamic studies of mixers for highly viscous shear thinning fluids and PIV validation

Marti Cortada-Garcia [a], Weheliye Hashi Weheliye [a], Valentina Dore [b], Luca Mazzei [a,*], Panagiota Angeli [a,*]

[a] University College London, United Kingdom
[b] GlaxoSmithKline Consumer Healthcare, United Kingdom

HIGHLIGHTS

- PIV mixing studies of highly viscous shear thinning fluids in stirred tanks.
- Computational fluid dynamic simulations of agitation of shear thinning fluids.
- Characteristics of flow using a complex impeller design.
- Study of local effect of holes in impeller blades.

ARTICLE INFO

Article history:
Received 12 September 2017
Received in revised form 29 November 2017
Accepted 7 January 2018
Available online 8 January 2018

Keywords:
PIV
CFD
Mixing tanks
Shear thinning fluids

ABSTRACT

Agitation of highly viscous shear thinning fluids is normally conducted with complex impeller designs. Often, impellers almost as large as the tanks containing them and impeller blades equipped with holes are adopted in industry. In this work, we studied experimentally the main features of the flow generated by this type of impellers for a mixture of glycerol with a carbomeric gel by means of particle image velocimetry. The experiments were conducted at temperatures ranging from 40 to 60 °C and impeller speeds ranging from 40 to 140 rpm. In all cases, the flow regime was laminar or in the transition region. We also used computational fluid dynamics simulations to describe the behaviour of the mixer, validating the results experimentally with good agreement. We used the numerical results to obtain information on the performance of the mixer, determining the locations and size of vigorous agitation zones and the local effect of the holes present on the impeller blades. The power curves of the mixer were obtained, and the mixer efficiency in terms of power consumption was found to be similar to other impellers used to mix highly viscous non-Newtonian fluids.

1. Introduction

Mechanically stirred tanks are ubiquitous in a wide range of chemical process industries. Their applications vary from mixing and blending different materials to generating solid suspensions or enhancing heat and mass transfer. Guidelines are readily available on the design of mixing tanks; these depend on the application, materials and volume to be mixed, and the flow regime (Kresta et al., 2015). Often these guidelines are based on industrial experience rather than on fundamentals and, as a result, extensive analysis and lab/pilot scale experimental studies are recommended to decide the best configuration for a particular application. These tend to be limited to low viscosity Newtonian fluids. In many industrial processes, however, the fluids to be mixed have high viscosity and non-Newtonian behaviour; for these the guidelines available for mixer design are not applicable.

The performance of mixers has been correlated to macroscopic properties such as power consumption of the impeller or mixing time. A number of studies can be found in the literature concerning these topics (see, for instance, Kazemzadeh et al., 2016, Patel et al., 2015, Stobiac et al., 2014, Guntzburger et al., 2013, Pakzad et al., 2013b). These overall parameters, however, do not reveal details of the fluid dynamics and mixing patterns within the mixers, which can only be obtained with detailed flow field measurements. Several experimental techniques have been developed to study the fluid dynamics in stirred tanks, including Laser Doppler Anemometry, Thermography, Tomography, and Particle Image Velocimetry (PIV) (Mavros, 2001). PIV is a non-intrusive technique that provides local multipoint velocity data at high spatial resolution. In the majority of cases it has been used to study mixing of simple Newtonian fluids, often water, with standard impeller designs

* Corresponding authors at: WC1E 6BT, United Kingdom.
E-mail addresses: l.mazzei@ucl.ac.uk (L. Mazzei), p.angeli@ucl.ac.uk (P. Angeli).

https://doi.org/10.1016/j.ces.2018.01.010
0009-2509/

(Sharp and Adrian, 2001, Baldi and Yianneskis, 2004, Montante et al., 2006, Delafosse et al., 2008, Gabriele et al., 2009, Zadghaffari et al., 2009). There are only few studies on the fluid dynamics of complex fluids in mixers operated in the laminar flow regime. The few available clearly demonstrate their importance in the development of mixer and impeller designs for viscous and non-Newtonian fluids. The Maxblend™ is one of such impellers; it was originally developed for mixing highly viscous fluids during chemical reactions (Hiruta et al., 1997) and it has been used in a wide range of industries, from production of PVC, biopolymers and biocellulose to surfactants across different scales (20-2500L) (Sumitomo, 2017). Fontaine et al. (2013) studied experimentally the effect of rheology on the fluid dynamics in a vessel with a Maxblend™ impeller using PIV and the decolorization technique for both Newtonian and non-Newtonian fluids (highly shear thinning and viscoelastic). Their results indicated that the performance of the impeller for highly shear thinning fluids is significantly worse compared to that achieved for highly viscous Newtonian fluids. Homogenization is even more difficult to achieve in viscoelastic fluids, which can rotate like a solid body with the impeller. Butterfly impellers, which are used to mix medium to highly viscous products, such as plasters, putties, adhesives and silicones, have also been characterized by means of PIV (Westerlins, 2016). Ramsay et al. (2016) studied the mixing of glycerol and of two viscoelastic Boger fluids (that is, fluids with constant viscosity but with elastic properties) with butterfly impellers, and found that these impellers are energetically more efficient than conventional Rushton and pitched blade turbines. However, their mixing performance is lower for viscoelastic fluids, because the latter tend to rotate as a solid body.

In addition to experimental studies, computational fluid dynamics (CFD) has been used extensively to investigate mixing in stirred vessels. The CFD models solve the fundamental balance equations of mass, linear momentum and energy in a discretized fluid domain. Similar to the experimental studies, the CFD investigations of laminar mixing of non-Newtonian fluids are very limited compared to the studies on mixing in general (49,000 compared to 20 publications). Validation of the CFD models is a major concern, and PIV studies have been used successfully for this purpose. Sossa-Echeverria and Taghipour (2015) found comparable velocity profiles from CFD and PIV for yield stress and shear thinning fluids stirred with three different side-entered axial flow impellers and evaluated the cavern formation around the impeller. Couerbe et al. (2008) studied the agitation of thixotropic shear thinning fluids exhibiting yield stress in vessels equipped with a Mixel TT agitator (axial impeller) both experimentally, by means of PIV, and computationally (ANSYS CFX) in the laminar regime. For the computations they used both the modified Hershel-Bulkley model (Zhu et al., 2005) and the Coussot model simplified for steady state flows (Coussot et al., 2002). The simulations agreed well with the experimental results; this indicates that simple models such as the Herschel-Bulkley can be employed to describe complex rheological behaviour such as thixotropy. The numerical simulations predicted the essential features of the flow, such as cavern formation, the locations of recirculation regions and the overall magnitudes of the velocities. Arratia et al. (2006) used PIV as well as Planar Laser Induced Fluorescence (PLIF) and Ultraviolet (UV) fluorescence to study velocity profiles and cavern formation during the mixing of glycerine and of a Herschel-Bulkley fluid (aqueous 0.1% Carbopol solution) with a centered triple Rushton turbine. They modeled the system with CFD, and found good agreement with the experiments. They observed strong compartmentalization due to the yield stress, and they concluded that the mixing of shear thinning fluids with yield stress is enhanced by breaking the symmetry of the impeller.

The manufacturing of oral health products involves many mixing steps of viscous non-Newtonian fluids. It is a challenge for the industry to be able to predict accurately mixing times of various components for different equipment set ups and materials properties. Usually longer than necessary mixing times are used to ensure that the mixing is complete; this decreases the efficiency of the process and increases operating costs. In addition, for non-aqueous mixtures in particular, long mixing times lead to product degradation and must be avoided. The rheology of the non-Newtonian mixtures depends on their composition, which is transient and non-uniform during mixing, while the mixing process is dominated by convection. It is very important therefore to correctly characterise the local fluid dynamics and flow in the stirred vessels and to develop a CFD model that accurately captures them. Validation of such a model using macroscopic experimental variables, such as overall power consumption, is not adequate and detailed flow information is needed. The objective of this work is to study the flow behaviour of a lab-scale mixer which includes the main features of industrial-scale agitators for the manufacturing of non-aqueous toothpastes. We implement a CFD model to study the agitation of non-Newtonian fluids with different rheological behaviour at different temperatures. We validate it against detailed PIV measurements of velocity profiles in a plane and indirectly test the rheological expression derived experimentally for this system.

2. Methodology

2.1. Rheology characterization

The test fluids used were glycerol and a gel made of polyethylene glycol (96%) and Carbomer (4%). The rheological properties of glycerol are available in the literature (Green, 2008). We previously reported on the rheological properties of mixtures of the same fluids (Cortada-Garcia et al., 2017). In this previous work we determined the viscosity of mixtures of glycerol and gel in the ranges of 1–250 s^{-1} shear rate and 25–85 °C temperature over the whole spectrum of mass fractions. In the current work we focused on mixtures with low gel mass fractions (5% and 20% gel in glycerol by weight) at temperatures ranging from 40 °C to 60 °C. As will be shown later in this article, the shear rate range previously reported is not broad enough for the present study; so, we expanded our previous rheological data to cover the shear rate range from 0.1 s^{-1} to 1000 s^{-1} which is representative of the range of shear rates encountered in the stirred vessel. For each set of conditions, the rheology was characterized at 20 equidistant points in a logarithmic scale (indicative results are shown in Figs. 1 and 2). Within the shear rate range investigated, the error associated with the accuracy of the instrument is negligible. The measurements were carried out in an Anton Paar Physica MCR 301 rheometer with parallel plate geometry. In this configuration, the shear stress is evaluated at the rim of the upper plate, where both shear stress and shear rate have maximum values.

We used the Carreau model to fit the rheological data:

$$\eta = \mu_\infty + (\mu_0 - \mu_\infty)[1 + (\lambda\dot{\gamma})^2]^{\frac{n-1}{2}} \quad (1)$$

where η is the non-Newtonian viscosity, μ_∞ is the viscosity on the plateau where the shear rate is very large (in the limit to infinity), μ_0 is the viscosity on the plateau where the shear rate is vanishingly small (in the limit to zero), λ is the time constant, $\dot{\gamma}$ is the magnitude of twice the rate of deformation tensor, and n is the shear thinning index. The error was computed for each individual point, and the mean error for a given composition and temperature was computed with the following expression:

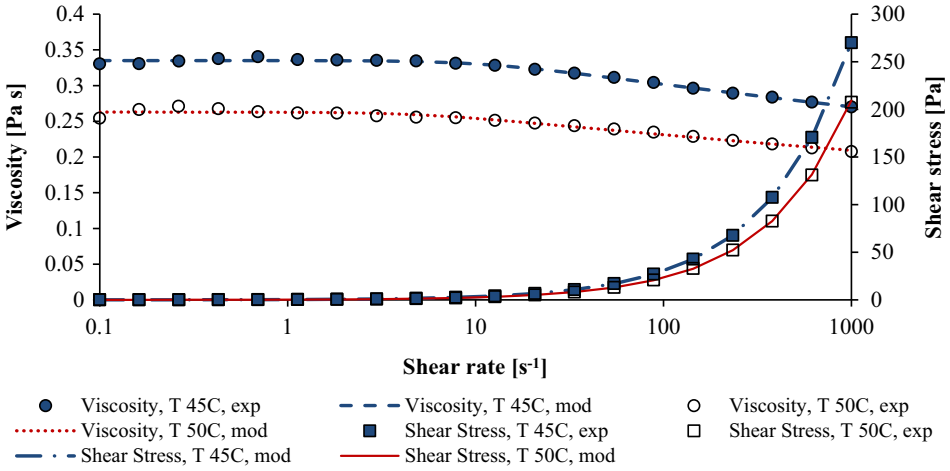

Fig. 1. Viscosity and shear stress as a function of the shear rate for the 5% gel mixture.

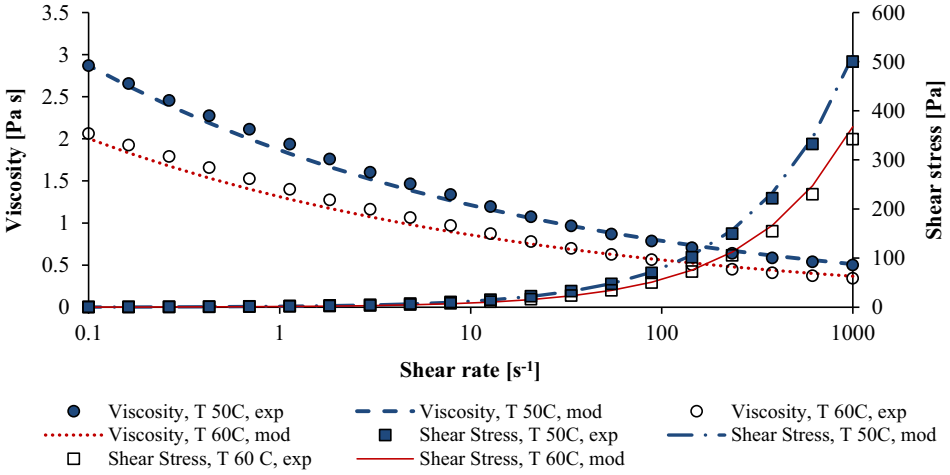

Fig. 2. Viscosity and shear stress as a function of the shear rate for the 20% gel mixture.

$$\text{Mean error } [\%] = \frac{1}{m}\left[\sum_{i=1}^{m}\frac{|x_{i,\text{exp}} - x_{i,m}|}{x_{i,\text{exp}}}\right]\cdot 100 \qquad (2)$$

The coefficients of the Carreau model together with the modelling error in the Carreau fitting for the experimental conditions studied can be found in Tables 1 and 2.

We also conducted oscillatory rheological measurements to determine the viscoelastic response of the 20% gel mixture, which is the fluid with the greatest gel mass fraction, and hence, it is the one that is expected to have the strongest elastic behaviour. For this test, we used the same parallel plate geometry, and we conducted amplitude sweep tests at constant frequency of 1 Hz for at the temperatures reported in Table 2. The results obtained for the case of 20% gel mixture at 50 °C are shown in Fig. 3. Similar curves were obtained for the same gel mass fraction at the other temperatures, and hence, they are not presented here. Fig. 3 reveals that the viscous response dominates over the elastic one, as the phase angle (δ) between the applied strain and the stress response is above 45° over the entire curve (Schramm, 1994). In some studies, the end of the linear viscoelastic region has been used to estimate the value of the yield stress (De Graef et al., 2011). Using this approach, the yield stress obtained with the results presented in Fig. 3 is approximately 0.1 Pa. This value is close to zero, which indicates that the yield stress is negligible for the fluids considered in this study. Because of the lower gel mass fraction, both the elastic behaviour and the yield stress for

Table 1
Parameters of the Carreau model and average error in the fitting for the 5% gel mixture.

T [°C]	λ [s]	n [ ]	μ_0 [Pa s]	μ_∞ [Pa s]	Error [%]
40	0.6000	0.9552	0.4767	0.0	1.81
45	0.0876	0.9520	0.3350	0.0	0.41
50	0.1930	0.9567	0.2628	0.0	0.92
55	0.4179	0.9593	0.2120	0.0	1.78
60	0.3109	0.9552	0.1707	0.0	2.56

Table 2
Parameters of the Carreau model and average error in the fitting for the 20% gel mixture.

T [°C]	λ [s]	n [ ]	μ_0 [Pa s]	μ_∞ [Pa s]	Error [%]
40	100	0.8208	6.253	0.0001	2.86
45	100	0.8147	5.304	0.0001	3.33
50	100	0.8126	4.423	0.0001	3.83
55	100	0.7987	4.239	0.0001	2.32
60	100	0.8158	3.063	0.0001	6.47

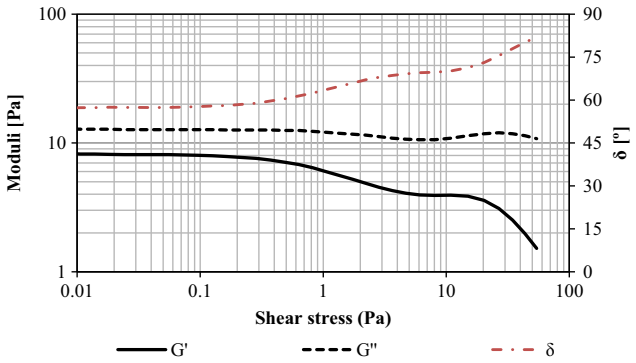

Fig. 3. Storage (G′) and loss (G″) moduli, and phase angle (δ) against the oscillatory shear stress for the 20% gel mixture at 50 °C.

the 5% gel mixture are expected to be even less significant compared to the 20% one. For these reasons, the Carreau model is suitable for the fluids studied here.

2.2. Experimental set-up

The mixing studies were carried out in a cylindrical acrylic tank equipped with a stainless steel dual impeller with two flat blades on each position and with two holes on each blade. The tank has two baffles that are used to generate high shear zones in the space between them and the impellers. A schematic of the tank and all the relevant dimensions are shown in Fig. 4. The liquid height corresponds to 14 cm. This geometry was chosen because it resembles that of industrial mixers for highly viscous fluids. The cylindrical tank is enclosed in a square tank, made of acrylic, which is filled with glycerol. The purpose of the outer tank is twofold: it is used to regulate the temperature within the stirred tank and to match the refractive index of the processing fluids (1.4675 and 1.4645 for glycerol and gel at 25 °C, respectively) and the solid vessel (1.4945) and avoid optical distortions on the surface of the cylindrical vessel. The glycerol in the square jacket is circulated by two pumps via a bath, which controls its temperature.

Velocity measurements were carried out using Particle Image Velocimetry. The PIV set-up includes a dual cavity Nd:Yag green laser (532 nm) (Litron Laser®, 15 Hz, 1200 mJ) and a straddling CCD camera with 2048 × 2048 pixels (TSI PowerView™ Plus) and a maximum frequency of 16 frames per second, equipped with an AF Nikkor 50 mm f/1.8D prime lens (Nikon®). A hall switch sensor was used to capture images at the same phase angle. We used fluorescent polymer particles (melamine resin based) coated with rhodamine B (20–50 μm) as tracer, which absorb in the green laser light. They are neutrally buoyant in the fluids considered, and, at the experimental conditions explored, their relaxation time is negligible compared to the convection time ($St \ll 1$). To ensure that only the emitted light from the particles (maximum emission at 590 nm) was recorded by the camera, we used an orange filter with a cut-on wavelength at 570 nm. The laser and the camera were synchronized by means of a Laser Pulse Synchroniser (Model 610035 TSI) and they were controlled via the Insight 4G (TSI) software. The laser beam was passed through a collimator (Model 610026 TSI) and two cylindrical lenses (25 mm, and 15 mm) to transform it into a narrow plane of 1 mm thickness. The generated laser plane was reflected on a 45° silver coated mirror and entered the stirred vessel from the bottom. To maximize the visualization area, we captured the velocity profiles on a vertical central plane of the tank, when the top blades of the impeller were parallel to that plane. A sketch of the setup is shown in Fig. 5.

In a typical experiment, we first filled the outer acrylic box with glycerol at the required temperature. The test mixture at the required concentration was pre-heated at the same temperature as the glycerol present in the outer box and then loaded in the stirred vessel. Subsequently, we started the impeller at 100 rpm and added the Rhodamine particles. We recorded ten images, to ensure that the tracer concentration was sufficient (about 4–6 particles per PIV correlation box). We then set the impeller at the required speed for the given experiment and captured the PIV images. The velocities converged when over 100 image pairs were averaged and for the results shown here we averaged about 200 images to minimize statistical errors.

Raw images needed to be treated before obtaining the velocity profiles. Images were processed in a greyscale, where zero is the equivalent of black, while the maximum value of the scale (in our case 255) corresponds to white. We first masked the impeller, and then we cropped the images at the edges of the tank and at the top of the fluid. We reduced the noise by setting a threshold below which the values of the pixels are set to zero (the colour is set to black). Then we re-scaled the intensity of the pixels to obtain sharper tracer images. The preprocessing was carried out in MATLAB. The images were then further processed with the freeware package JPIV. A 50% window overlap was used for a final resolution of 16 × 16 pixels, corresponding to an area of 1.6 × 1.6 mm^2. The spurious vectors were removed and an amplitude filter was applied to each cross-correlation box to eliminate the vectors that substantially deviate from the median value (smoothing) (Westerweel and Scarano, 2005). Then, on each cross-correlation box, we calculated the average and the standard deviation over the total number of images. For the case shown in Fig. 6, for a gel concentration of 5%, the total uncertainty in calculating the velocity vector was 0.0006 m/s, which is the equivalent of 1.5% for high velocity regions.

The PIV errors were estimated using the bias limit formula (Moffat, 1988). After considering all the potential sources of error (Adrian and Westerweel, 2011), we concluded that both the sampling and the interrogation errors were relevant to our PIV study. Fig. 6 shows the average PIV velocities and estimated error in all the cross-correlation boxes across the Z direction at a given Y position.

2.3. CFD modelling strategy

As shown in Fig. 4, the height of the fluid in the vessel was set at 14 cm. This is 2.3 cm above the highest blade. Because of the baffles, the interface remained flat in all the experiments. To avoid using multiphase models, we simulated only the region occupied by the fluid, which extends from the bottom of the tank up to a

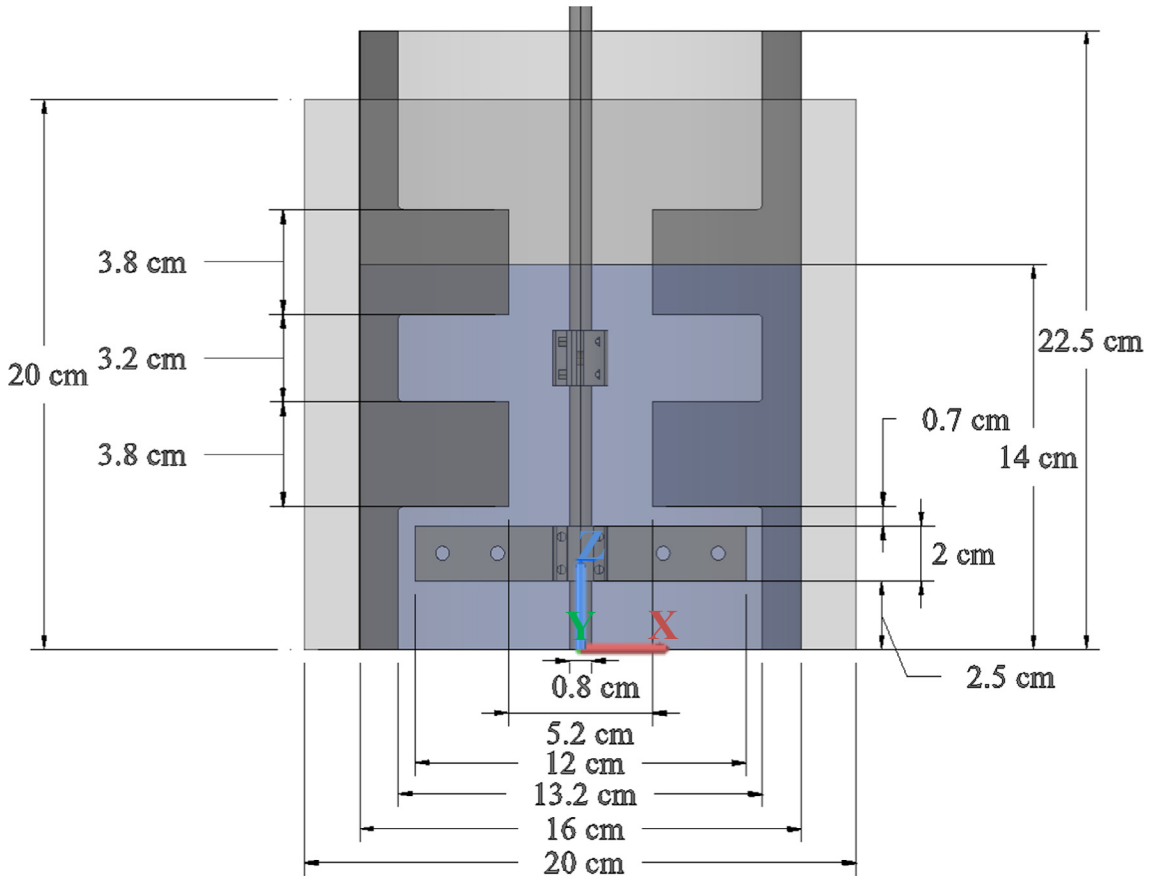

Fig. 4. Schematic and dimensions of the tank, impeller, baffles, and liquid height.

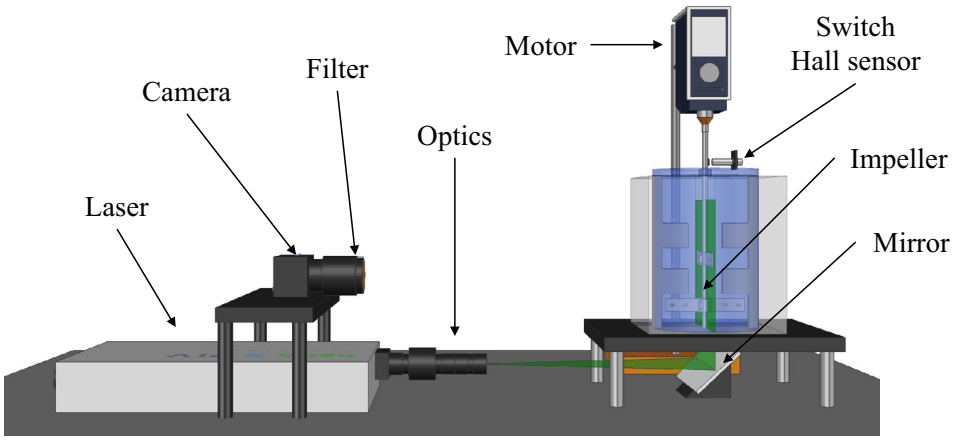

Fig. 5. Sketch of the main components of the experimental set-up for the PIV measurements.

height equal to 14 cm. At the top boundary, where the liquid-gas interface lies, the components of the viscous stress force referring to the unit vector normal to the interface were set equal to zero. Additionally, on all the solid surfaces bounding the computational domain, the no-slip boundary condition was applied.

Due to the small distance between the impeller and the walls of the tank and the baffles, the only appropriate modelling approach is the Sliding Mesh (SM). The Reference Frame approach can only be used to initialize the fluid motion. In the SM approach, the geometry should have at least two connected non-deforming zones that slide in relation to each other. All the moving parts (in this case, the impeller) need to be part of the moving zone. In the present study, we employed as moving zone the union of three cylinders, one enclosing the shaft of the impeller and two enclosing one of the two impellers each. These three cylinders are merged as a single rotating zone. The cylinder enclosing the shaft has a diameter of 2 cm. The boundaries of the cylinders surrounding the top and bottom blades were defined at the midpoint between the tip of the blades and the edge of the baffles. The elements outside these cylinders formed the stationary zone. A graphical representation of this can be seen in Fig. 7, where the yellow and blue regions correspond to the moving and stationary zones.

The computations were carried out in ten parallel processors using a 3.10 GHz Intel® Xeon ® CPU E5-2687 W v3 with 192.0 GB

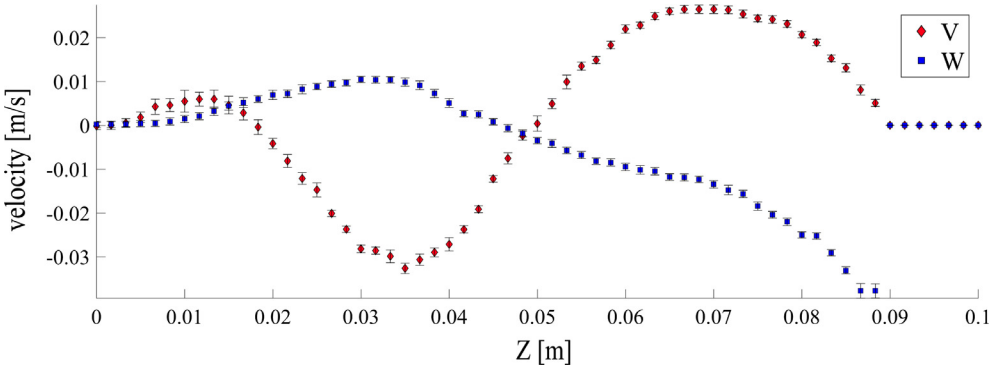

Fig. 6. Experimental profiles of the y- and z-velocity components (V and W respectively) with error bars along the Z-direction for Y = −0.053 m, and X = 0 m, for 5% gel and 40 rpm.

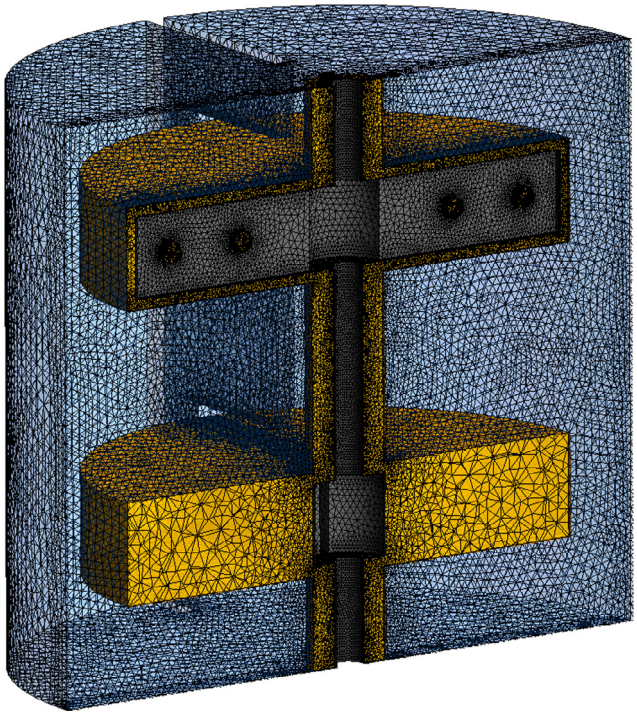

Fig. 7. Schematics of the moving (yellow) and stationary (blue) zones. The final grid can also be seen. (For interpretation of the references to colour in this figure legend, the reader is referred to the web version of this article.)

RAM. The tank and impeller were drawn with AutoCAD. The different meshes were created with ANSYS Workbench. Unstructured meshes were preferred because of the shape of the impeller. The fluid dynamic model was solved using ANSYS Fluent 16.1. Different numerical schemes were tested and the combination selected was the one that provided the fastest convergence with accurate results. We set up the solution methodology as follows: we used for pressure and velocity coupling the Coupled strategy, for spatial discretization the least squares scheme to evaluate the spatial derivatives, the second order interpolation scheme for the pressure, and the second order upwind scheme for the momentum. For the steady-state simulations (initialization only), we let the solver run until a plateau was observed on the scaled residuals of the continuity equation, and of the three velocity components. For transient simulations, we set 1° of impeller rotation per time step; the time step depends on the rotational speed assigned to the impeller, so that 360 time steps were equivalent to a revolution in all cases. The simulation is converged when the residuals reach a plateau, as in the steady-state simulations.

2.4. Grid-independence

The computational solution depends on the grid used in the simulation, if the grid is not fine enough; very fine grids, however, are computationally more demanding than coarser ones. So, before running the simulations, we attempted to determine a grid size that provides an acceptable trade-off between grid-independence and computational cost. We carried out simulations using three different grid sizes for a mixture with 5% gel at 49 °C and 40 rpm impeller speed. We compared the solutions for the four different mesh qualities by plotting the velocity profiles along the positive part of the y axis at different heights in the tank (z_1 = 3 cm and z_2 = 8 cm) on the central plane (x = 0 cm) where the top impeller blades are parallel to the plane (and consequently, perpendicular to the baffles and the lower blades). The details of the simulations are summarized in Table 3.

As can be seen in Fig. 8, the BQ and LQ meshes are not fine enough. The MQ and HQ provide almost identical results in all profiles presented in Fig. 8; this indicates that the solution has become nearly grid-independent. The MQ mesh was chosen because of the more time efficient performance. Simulations with the same four grids were repeated using the 20% gel mixture rotating at 140 rpm, and the same conclusions were drawn.

2.5. Post-processing

The mesh used in our CFD model is unstructured. In contrast, the PIV results are obtained in a structured grid defined by the cross-correlation box size. Consequently, the number and position of the CFD cells along the central plane of the vessel are different to those of the cross-correlation boxes of the PIV. To enable direct comparison, the PIV grid was adopted. The CFD results were modified by averaging the velocity values in the CFD cells occupying the space of a single PIV cross-correlation box. The procedure was carried out in MATLAB. An example is shown in Fig. 9.

Table 3
Summary of the meshes studied, number of cells and simulation time per mesh size.

Mesh	# Cells	Simulation time [days]
Bad quality (BQ)	36,000	<1
Low quality (LQ)	750,000	1.5
Medium quality (MQ)	1,600,000	3
High quality (HQ)	2,900,000	6

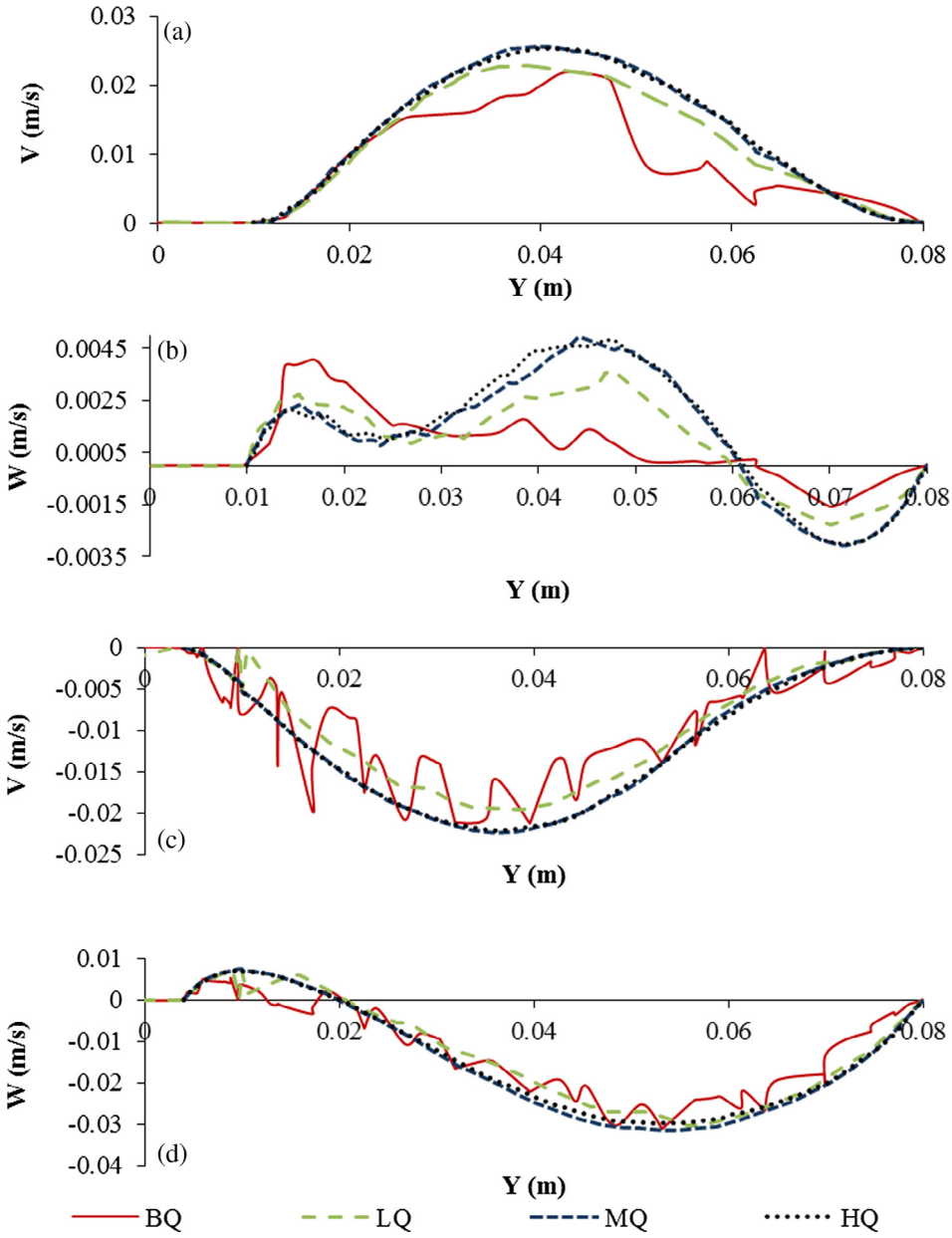

Fig. 8. Profiles of the y- and z-velocity components (V and W respectively) along the positive Y direction at X = 0 at two different heights (a and b) Z = 3 cm, and (c and d) Z = 8 cm.

2.6. Quantification of uncertainty between simulations and experiments

A number of considerations should be taken into account when comparing the CFD simulations and the experimental data from the PIV measurements. These are discussed below.

(i) Plane of measurement

With CFD it is possible to extract velocity data at any plane in the stirred vessel. However, in the PIV measurements, velocity is calculated from the displacement of particles over a certain (very short) time interval. Over this time interval, the impeller blades move. Consequently, to compare velocities between CFD and PIV, one needs to average the data from CFD over the region corresponding to the small displacement of the impeller during the PIV measurements. For example, for the velocities in the central vertical plane of the vessel that is parallel to the top blades and perpendicular to the lower blades and the baffles (coordinates: x = 0, y = [−0.08, 0.08] m, z = [0, 0.14] m), the PIV image pairs are over two planes, one just in front and one just behind the blade (see Fig. 10). The velocities from the CFD simulations need to be averaged over the region bounded by these two planes.

(ii) Plane misalignment

The laser was aligned by drawing two marks at two diametrically opposite points at the top of the tank, where the light should pass through (points A and B in Fig. 11). These are thin marks with 5 mm thickness; so, the uncertainty in the position of the laser plane is ±2.5 mm on both extremes. An exaggerated representation of this is shown in Fig. 11, P2 and P3. Also, the ideal plane alignment is shown in Fig. 11 as P1. In Fig. 11, the mixing tank is shown from above, the laser plane is plotted in green, the baffles

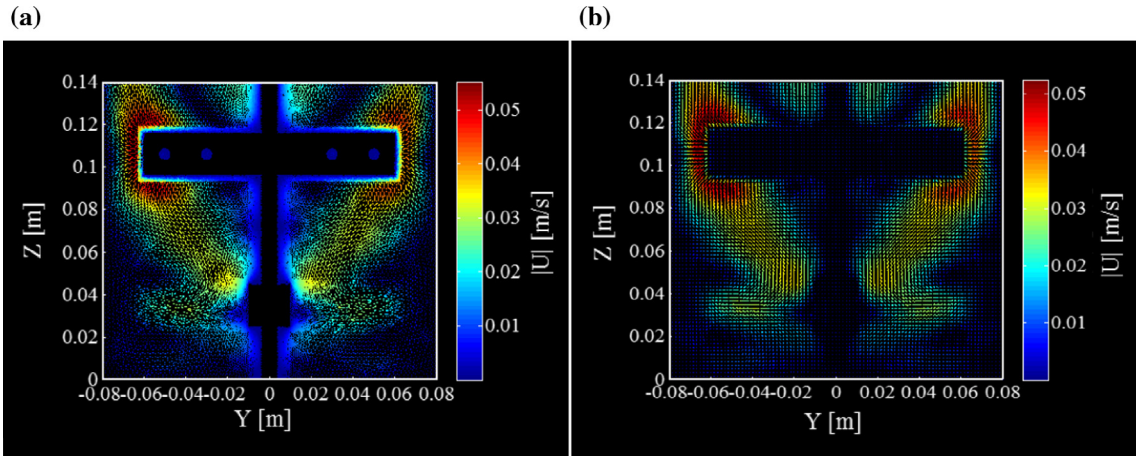

Fig. 9. Transformation of velocity results from the CFD to the PIV grid (a) velocities from the CFD simulations and (b) velocities translated into the PIV grid. 5% gel at 49 °C rotating at 40 rpm.

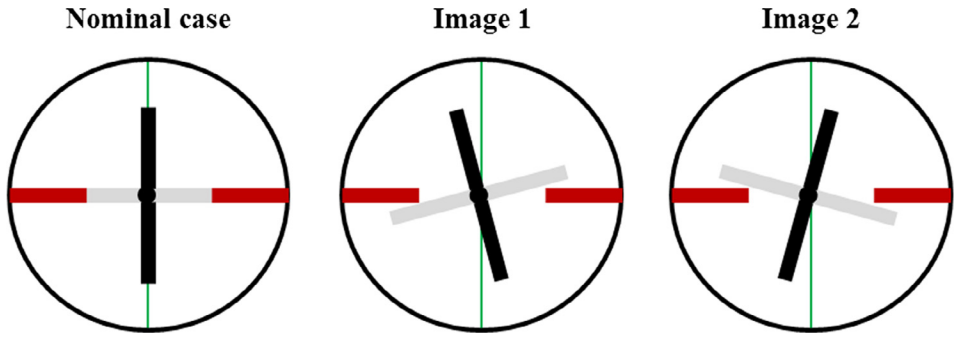

Fig. 10. Nominal case and position of impeller on PIV images (clockwise impeller rotation).

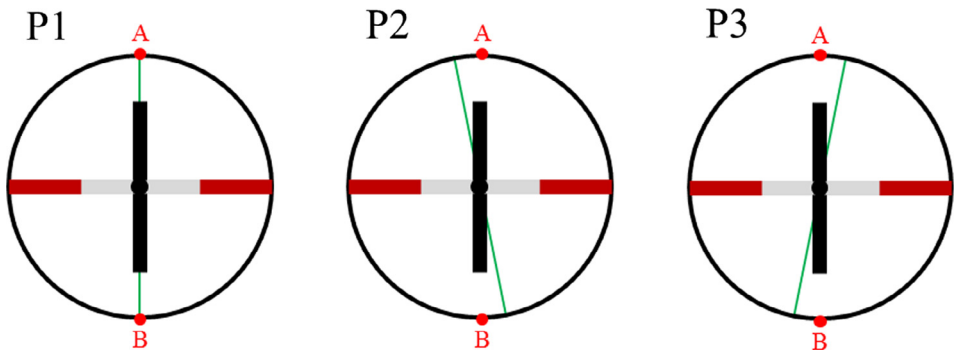

Fig. 11. Top view of the mixing tank and the effect of uncertainty in laser alignment.

are plotted in red, the top impeller is plotted in black, and the lower impeller is plotted in grey. The CFD results are extracted on the three planes, the velocity profile on P1 corresponds to the nominal case, and P2 and P3 are used to obtain a range of uncertainty for the CFD results. The PIV results are expected to fall within this range of uncertainty.

(iii) Synchronization of the switch hall sensor

We used a switch hall sensor to synchronize the laser pulses with the impeller rotation in the vessel and acquire images always at the same phase angle. We attached a magnet to the impeller, which triggers the laser and the camera when it is close enough to the sensor. Knowing the rotational speed of the impeller, and the Δt between the laser pulses, it is possible to calculate the phase angle difference between the two PIV images in a pair. For the case of 5% gel at 49 °C and an impeller rotating speed of 40 rpm, the Δt was 15 ms, which translates into a phase angle difference of 3°. The ideal scenario was presented in Fig. 11. Mispositioning the magnet changes the phase angle at which the images are captured. Exaggerated scenarios with delayed and prompt image acquisition are presented in Fig. 12(a) and (b) respectively. Based on our PIV results, the images that we acquired had a slight delay. The maximum delay observed in the images corresponds to that of the first image capturing the impeller on the center of the plane (this is pictured in Image 1 in Fig. 12(a)). In other words, the delay in our images is half of the phase angle difference between the PIV images. Consequently, we extracted the CFD results not only for

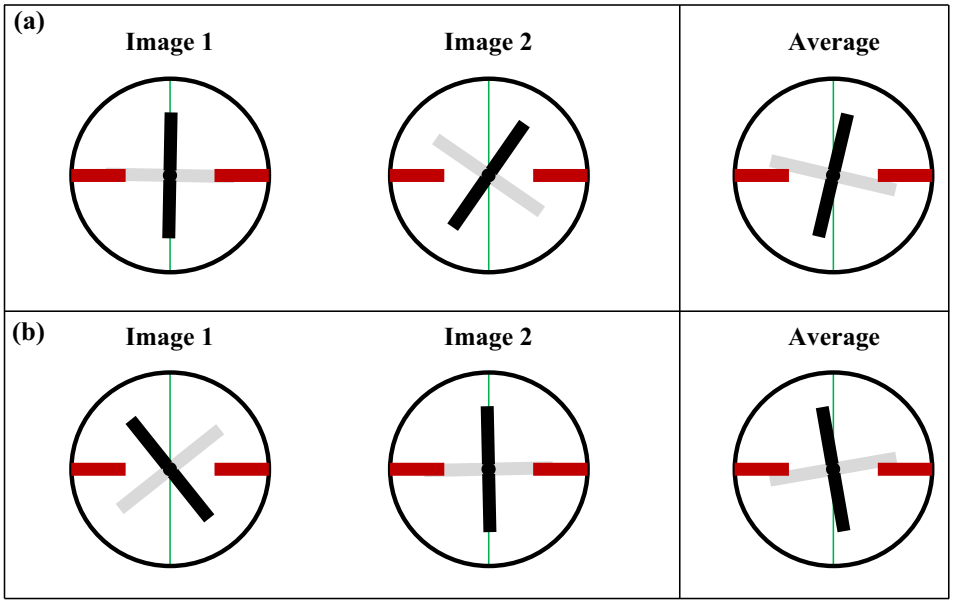

Fig. 12. Scenarios of mispositioning the sensor/magnet with clockwise impeller rotation; (a) delayed images scenario, and (b) prompt images scenario.

the nominal case, but also for the impeller positions corresponding to the delayed images, and we included these in the uncertainty on the CFD results.

(iv) Temperature

There were small variations of the temperature within the stirred vessel. For each set of conditions, we measured the temperature with a thermocouple throughout the experiment, and in the simulations we used both the highest and the lowest temperatures recorded.

The above uncertainties do not appear in isolation. Although they are experimental uncertainties, they cannot be accounted as experimental error bars. However, ignoring these may lead to discrepancies between the CFD and the PIV results. Therefore, we present the CFD results that correspond to the nominal PIV case as if the experiment was ideal, and we ascribe a range of uncertainty to the CFD results that corresponds to the maximum and minimum velocity values calculated considering all the sources of experimental uncertainty. In total, there are eighteen possible combinations of uncertainties accounting for the plane of measurement, plane misalignment, synchronization of the switch hall sensor, and temperature (excluding the nominal case) per experiment. For each experiment, we obtained the CFD results for all these combinations, and we translated the results into the PIV grid as explained in Section 2.5. Finally, we kept the maximum and minimum velocities of all the combinations in each position of the PIV grid. These denote the uncertainty in the CFD results owing to the imperfection in the experimental conditions. We consider that there is good agreement between simulations and experiments when the experimental velocities fall within the range of the uncertainty considered for the CFD simulations.

3. Results and discussion

3.1. Comparison of computational and experimental results

We studied the fluid dynamics in the stirred vessel for two different mixtures, gel 5%/glycerol 95% and gel 20%/glycerol 80%, for the impeller speeds reported in Table 4. The second mixture has a stronger non-Newtonian behaviour than the first, as shown in Section 2.1. Table 4 also reports the initial and final experimental temperatures (Ti and Te, respectively) as well as the time difference between the two PIV frames, the speed of the tip of the blades and the value of the Reynolds number defined in Eq. (3) and calcu-

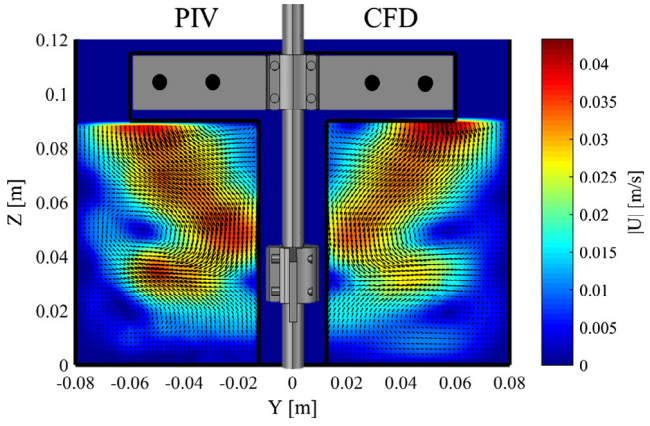

Fig. 13. PIV vs CFD velocity profiles on the plane X = 0 using the y- and z-velocity components for 5% gel and 40 rpm.

Table 4
List of experimental conditions.

Gel mass fraction [%]	N [rpm]	Ti [°C]	Te [°C]	T avg [°C]	Δt [ms]	Tip speed [m/s]	*Re* [ ]
5	40	50	48	49	15	0.25	38
5	120	48	46	47	6	0.75	120
20	80	60	58	59	12	0.50	23
20	140	52	51	51.5	6	0.88	44

lated by means of the Metzner and Otto approach (Metzner and Otto, 1957) (calculated constant of the impeller k = 15).

$$Re = \frac{\rho D^2 N}{\mu_\infty + (\mu_0 - \mu_\infty)[1 + (\lambda k N)^2]^{\frac{n-1}{2}}} \quad (3)$$

In Fig. 13, we compare the velocity profiles obtained experimentally and computationally on the YZ plane for the first case in Table 4. The left-hand side corresponds to the experimental results, and the right-hand side to the computational results corresponding to the nominal case presented in Fig. 11, P1.

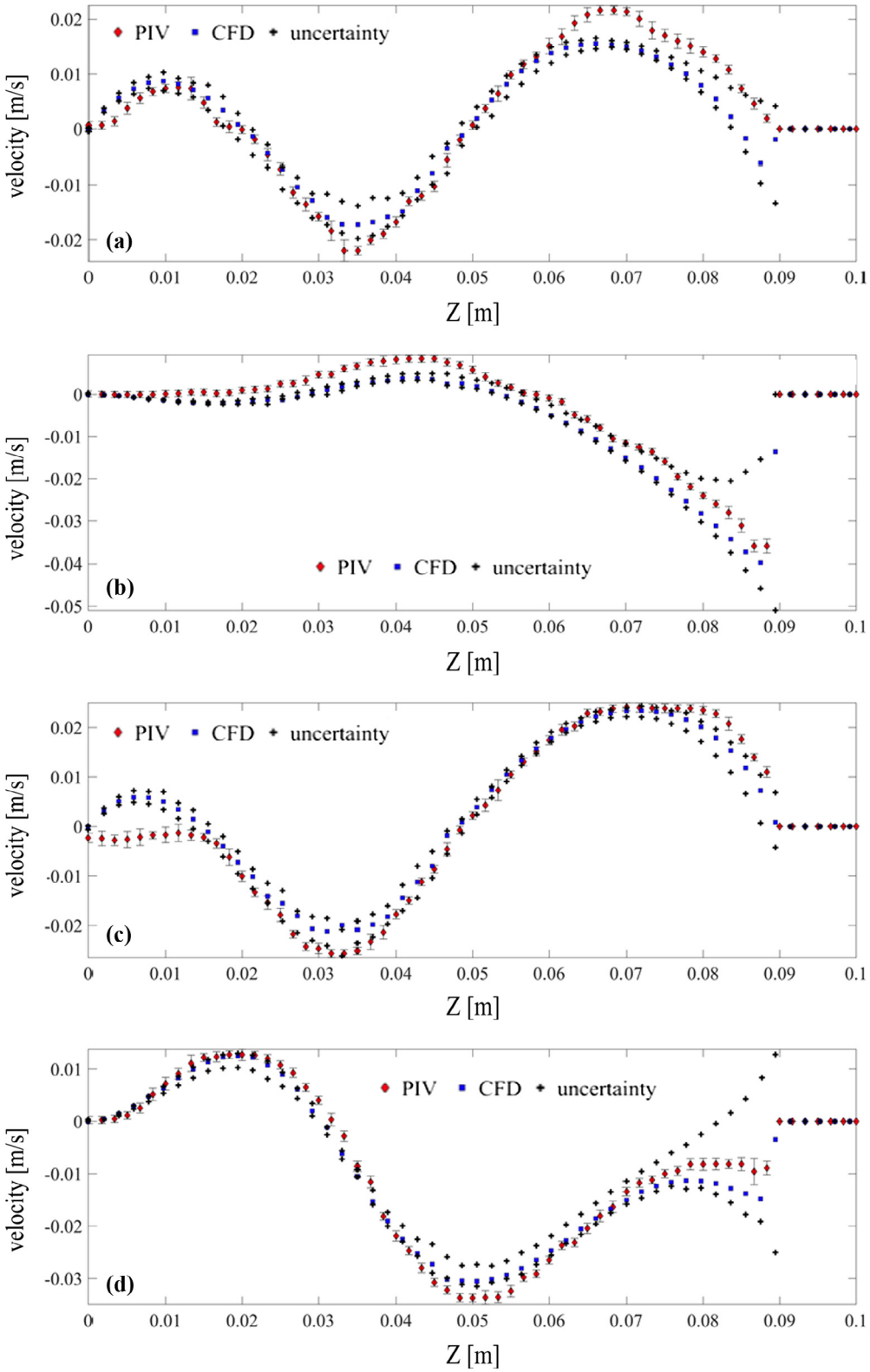

Fig. 14. Velocity profiles of V (a and c) and W (b and d) at two different Y positions [6 cm in (a and b), and 3 cm in (c and d)] along the Z direction for 5% gel and 40 rpm.

As we can see, the CFD is able to capture the main features of the flow; these include high axial downward velocities below the top blade and above the lower blade, and dominant radial velocities at the level of the lower blade. The CFD also predicts the location and magnitude of the vortex formed between the heights of 0.04 and 0.06 m, and the location of the quasi-stagnant zones near the lateral walls and the bottom of the tank. For a more detailed comparison, we selected two different Y positions in the tank (for X = 0), and we plotted the y and z velocity components (denoted as V and W) from both experiments and simulations along the Z direction in Fig. 14. In addition, we included the estimated error bars for the PIV results, and we accounted for the uncertainties in the comparison between experimental and computational results as explained in Section 2.6.

It can be seen in Fig. 14 that the computational and experimental values have similar trends. Some experimental points fall outside the CFD range, even when all the uncertainties are accounted for. However, in most cases, the deviation is small. It is important to notice that, in most of the profile, the uncertainties introduced by experimental imperfections, represented by black crosses, are small, and it is mainly near the blades (from 8 cm to 9 cm and from 2.5 to 4.5 cm) that these are significantly magnified. One could expect this, since the fluid is highly viscous. The highest velocities and the sharpest velocity gradients are localized near the moving objects; hence, small variations in the position of the blades and the recording plane have a significant impact on the local velocity vectors (as can be seen in Fig. 14(a)–(d)). In both cases presented in Fig. 14, the uncertainty of the z velocity component (W) is largest near the top blade. It is also in these regions that the CFD under-predicts the values of the velocity components. The greatest experimental error bars relative to the velocity are found in zones with low velocity; this is near the walls and bottom of the tank ($Z \cong 0$), where the relative error can be orders of magnitude above 100%. This is probably caused by the difficulty in capturing these velocity vectors due to loss of correlation of the PIV images (when the displacement of the tracer particles is smaller than 0.1 pixels in a pair of PIV images). This is particularly evident in Fig. 14(c), where one should trust the CFD predictions more than the experimental results near the bottom of the tank.

The same comparisons are also done for the 20% gel mixture for impeller speed 140 rpm, which has a similar value of the Reynolds number. The velocity profiles from both PIV and CFD are shown in Fig. 15, while the V and W velocities along Z are shown in Fig. 16 for two Y positions.

From Fig. 15 we can see that there is overall good agreement between the experimental and numerical velocity profiles. The flow has similar characteristics to the previous case, with strong downward velocities near the top blades and above the lower blades, and high radial velocities near the lower blade. In this case, however, vortices between the heights of 0.04 and 0.06 m are not formed; instead, the low velocity zones are larger in this case, and they occupy that space. Focusing in Fig. 16, we can see that also in this case the CFD is able to capture accurately the experimental velocity profiles. The uncertainties in the CFD simulations are small for most of the profiles, although near the blades these are magnified. The greatest uncertainties for W are found near the top blades, while for V near the lower blades (heights of 0.025–0.045 m). Similar to the previous case, the velocity vectors near the walls of the tank, and in particular those near the bottom ($Z \cong 0$), are subject to the greatest experimental relative error. The overall velocity profiles of the two remaining cases are presented in Fig. 17(a) and (b), and very similar conclusions can be drawn.

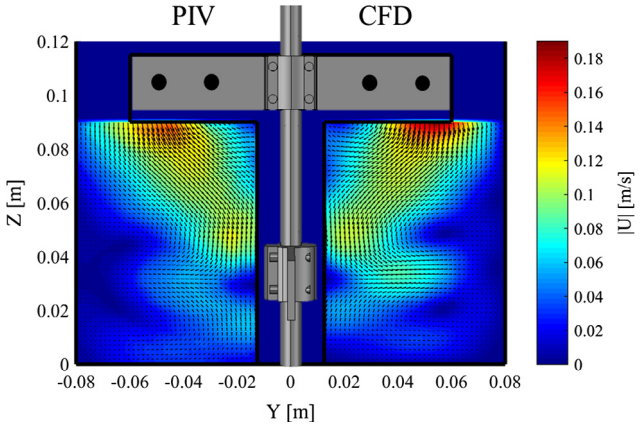

Fig. 15. PIV vs CFD velocity profiles on the plane X = 0 using the y- and z-velocity components for 20% gel and 140 rpm.

3.2. Flow in the vessel

We can use the validated CFD model to study the characteristics of the flow in the whole vessel. The previous results revealed that the velocities in the y and z directions, and consequently their magnitude too, are significantly smaller than the tip speed (about 10% of the tip speed near the top blade). This indicates that this type of impeller provides little radial and axial flow motion compared to the angular flow motion. This can be shown by plotting the three-dimensional streamlines at the same impeller position used in the PIV experiments for the case of 5% gel mixture and 40 rpm impeller speed (Fig. 18).

As can be seen in Fig. 18, the highest velocities are found adjacent to the tip of the blades, and the velocity decays rapidly away from the impeller because of the high viscosity of the fluids; nevertheless, the streamlines reveal that there is circulation of the fluid in the entire tank, with only few stagnant areas (those with zero velocity) near the bottom of the tank and adjacent to the baffles. The streamlines also reveal that there is top to bottom recirculation, but the velocity magnitude is significantly smaller compared to the tip speed. As mentioned before, the dominant motion is in the angular direction. The streamlines for the 20% gel mixture stirred at 140 rpm (Fig. 19) reveal similar patterns: strong angular velocity compared to the radial and axial ones, and velocity decay away from the impeller. In this case, however, the velocity decays even faster with distance from the impeller, as the fluid has stronger shear thinning behaviour (smaller n) and higher viscosity compared to the 5% gel case. This creates a pseudo-cavern around the impeller, which is surrounded by quasi-stagnant fluid.

Intuitively, for shear thinning fluids, desirable mixer design criteria should involve good propagation of the fluid motion to the largest part of the vessel. This can be assessed by setting different velocity thresholds (fractions of the tip speed), and determining the percentage of the fluid volume that moves at higher velocity than the thresholds. We show in Fig. 20 the isosurfaces of velocities equal to 10%, 30%, 50% and 70% of the tip speed for a 5% gel and 40 rpm impeller speed. As can be seen, the velocity decays very rapidly away from the impeller. In particular, the highest velocities, those above 70% of the tip speed, are only found in close proximity of the tip of the blades (Fig. 20(d)). Fluid with velocities above 50% of the tip speed is only found along the blades and in a small region behind the tip of the blades (Fig. 20(c)). The impeller, however, is able to prevent the formation of stagnant zones under the conditions studied (Fig. 20(a)). The narrow gap between the blades and the baffles increases locally the shear rate, thus reducing the fluid viscosity; as a result, the fluid velocity between the low blades and the baffles is comparatively large (Fig. 20(b)).

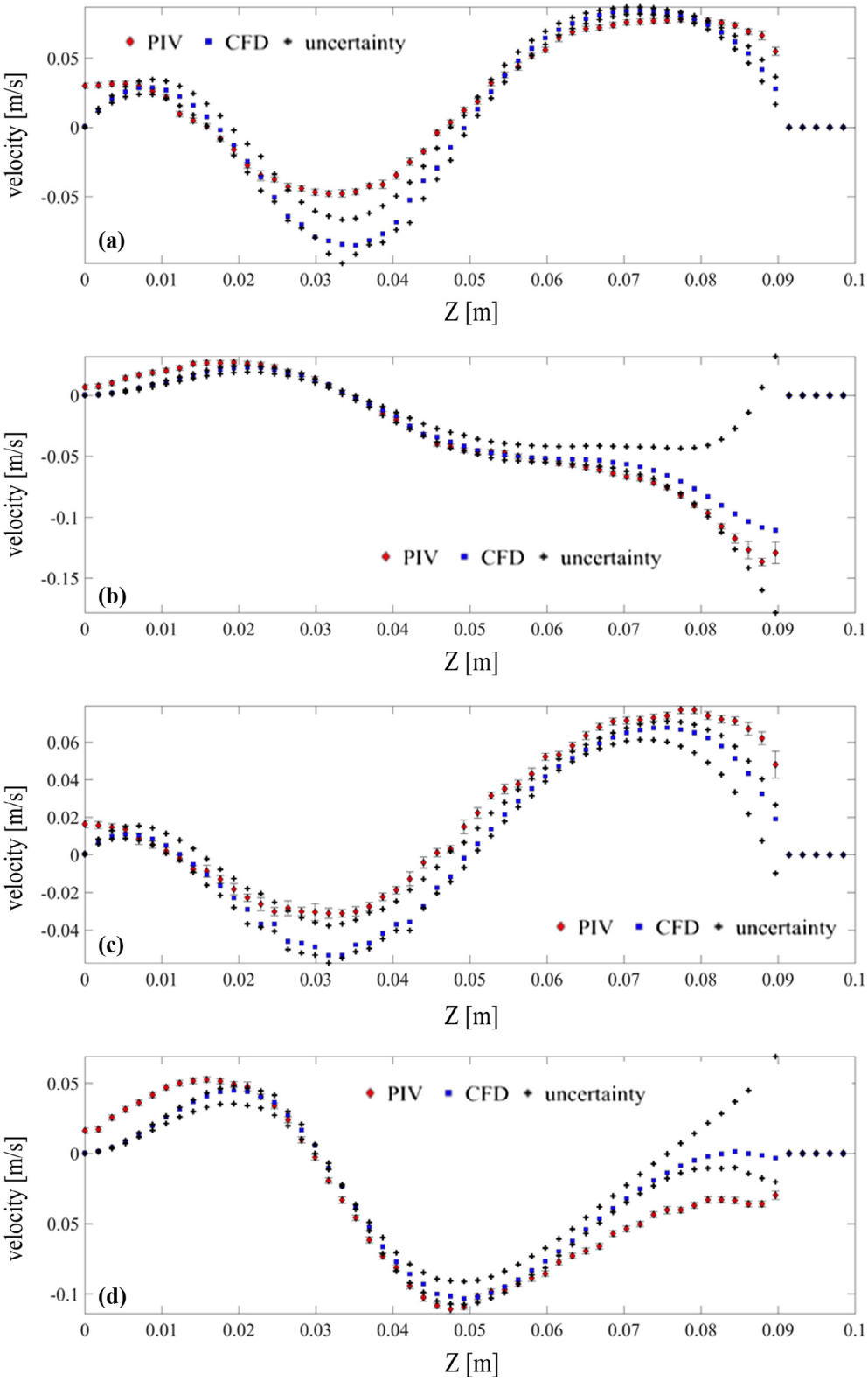

Fig. 16. Velocity profiles of V (a and c) and W (b and d) at two different Y positions [4.4 cm in (a and b), and 2.3 cm in (c and d)] along the Z direction for 20% gel and 140 rpm.

Quantitative information can also be obtained by extracting the fluid velocity magnitude in each computational cell, and plotting a histogram of the volume fraction of the fluid that has certain velocity relative to the tip speed (Fig. 21). The cumulative volume fraction of the histograms for all cases studied is also presented in Fig. 21. The profiles do not change significantly with the phase angle of the impeller. In all cases, low velocities relative to the tip speed are dominant. The cumulative plot is particularly helpful to identify the configurations that provide more efficient propagation of motion from the impeller to the fluid; these are denoted by a slow increase of the cumulative volume fractions against the relative velocity. If we compare the two cases of the 5% gel, we see

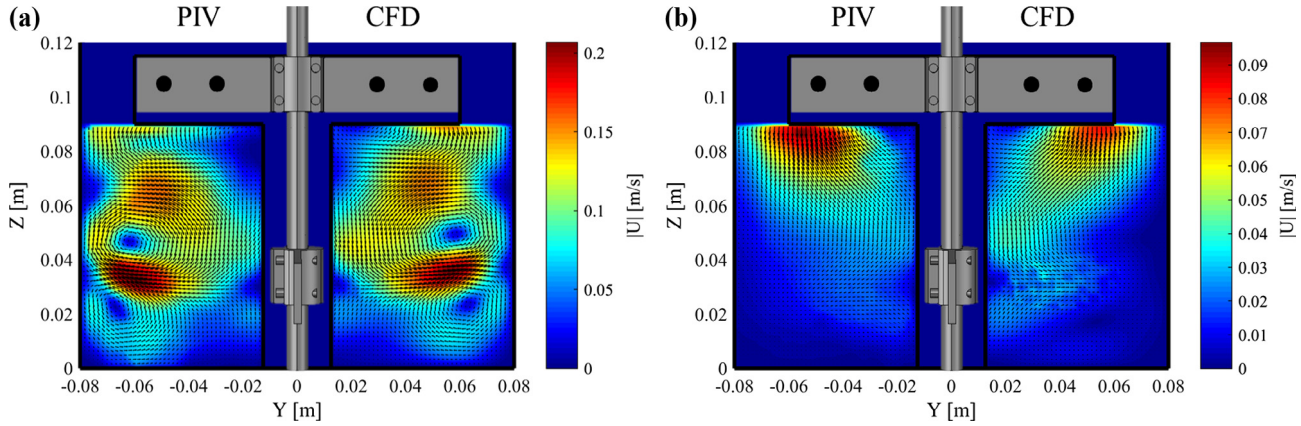

Fig. 17. PIV vs CFD velocity profiles on the plane X = 0 using the y- and z-velocity components for 5% gel and 120 rpm (a) and 20% gel and 80 rpm (b).

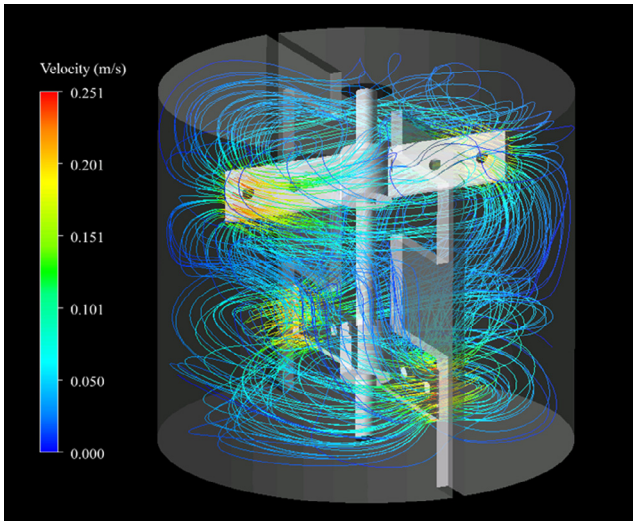

Fig. 18. Velocity streamlines for 5% gel and 40 rpm.

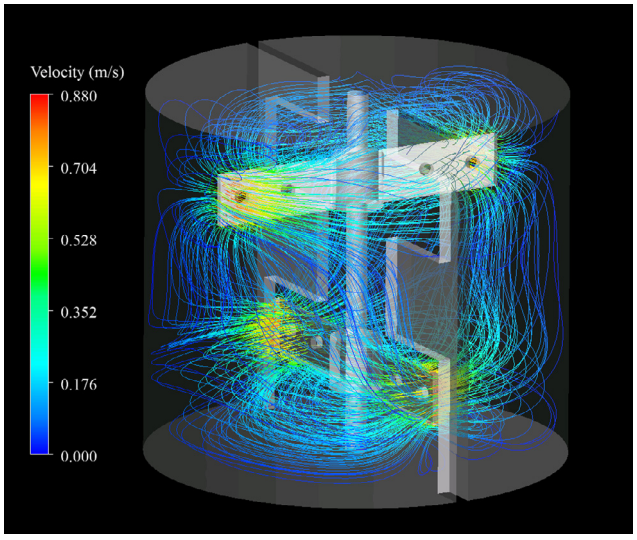

Fig. 19. Velocity streamlines for 20% gel and 140 rpm.

that the cumulative curve increases faster at 40 rpm compared to 120 rpm, which means that more fluid in the vessel has a low velocity relative to the tip of the blades at 40 rpm compared to 120 rpm. The two cases studied with 20% gel are also shown in Fig. 21; in this case there is no noticeable improvement in the efficiency of the mixer when increasing the rotational speed from 80 to 120 rpm. Overall, the performance of the mixer is better for the lower gel mass fraction, regardless of the impeller speed. From Fig. 21 we conclude that this impeller and baffles designs are not particularly efficient to agitate highly viscous shear thinning fluids.

3.3. Effect of the holes

Holes on impellers are unique design features for some mixers treating highly viscous non-Newtonian fluids. Their purpose is related to a mechanical standpoint: they enhance stability of large impellers, and reduce the pressure on the blades, thereby reducing power consumption (STC Engineering, Personal communication). However, to the best of the authors' knowledge, their effect on the fluid flow has not been studied. To do so, we plot the shear rate profiles (profiles of the magnitude of twice the rate of deformation tensor) on the front of the top blade and the viscosity contours for the cases of 5% gel and 40 rpm and 20% gel and 140 rpm in Fig. 22 (a) and (b), respectively. Similar results are found for the remaining configurations. As can be seen, the highest shear rates are found along the edges of the impeller blade, and particularly at the tip. The shear rate on the front face of the blade is lower than that on the edges, and it increases from the center to the tip of the blade. The presence of the holes reduces the surface of the blade and increases its perimeter, thus increasing the total length of the edges of the impeller, and therefore the local shear rate (Fig. 22). For shear thinning fluids, increasing the shear rate locally is beneficial to enhance flow, since the viscosity of the fluid is reduced locally, and consequently the local velocity is increased. However, the impact of these particular holes on the fluid dynamics is almost insignificant, and we conclude that in this case, the holes are solely justified from the mechanical standpoint.

Overall, the shear rate ranges from 0.1 s^{-1} to 200 s^{-1} for the 5% gel and 40 rpm case (Fig. 23(a)) and from 0.1 s^{-1} to 900 s^{-1} for the 20% gel and 120 rpm case (Fig. 23(b)). This proves that the shear rate range investigated in the rheological study presented in Section 2.1 was adequate for our simulations. The shear rate profile on both the bottom and top blades is practically identical. However, the shear rate profile on the baffles changes with the relative position of the impeller. In the case shown in Fig. 23(a) and (b), the bottom blades are passing through the baffles, and the shear rate on the baffles increases locally near the bottom blade. This can be linked to Fig. 20(b), where the fraction of fluid that has a velocity above 30% of the tip speed is greater around the lower blade compared to the top blade.

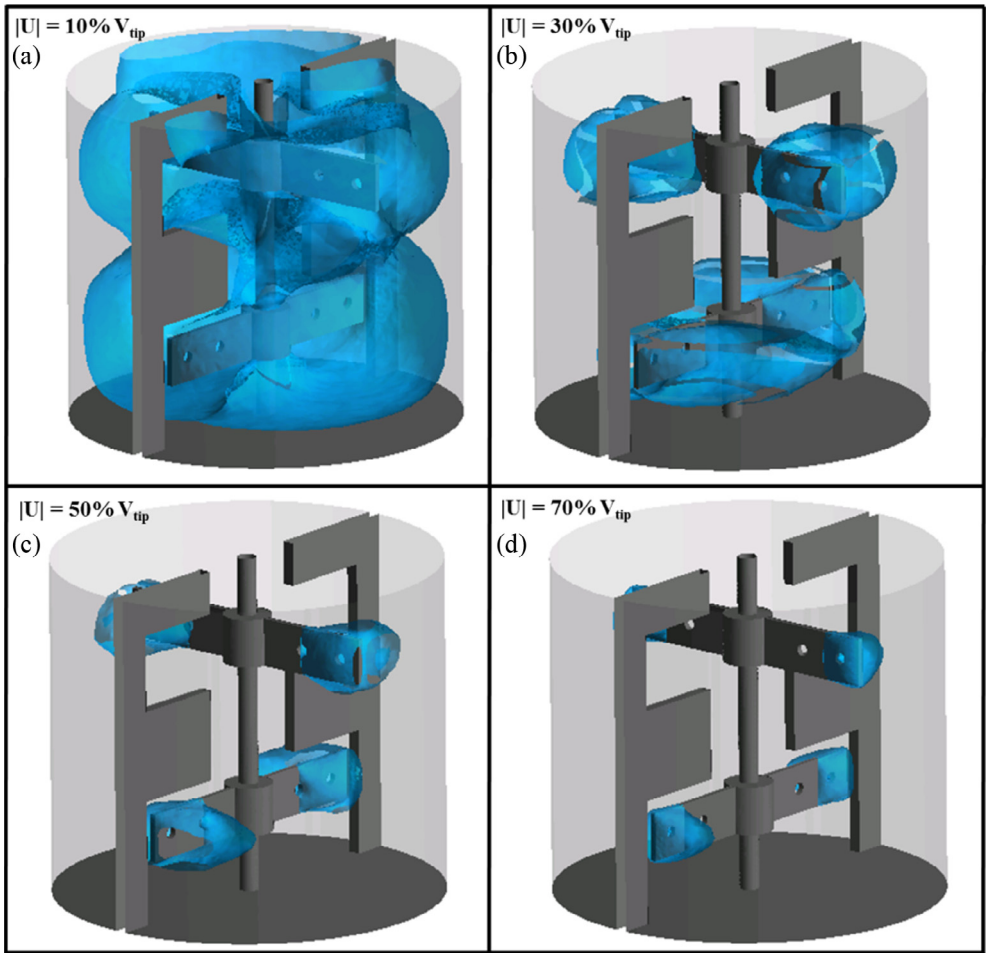

Fig. 20. Isosurfaces of velocities as fractions of the tip speed, (a) 10%, (b) 30%, (c) 50%, and (d) 70%.

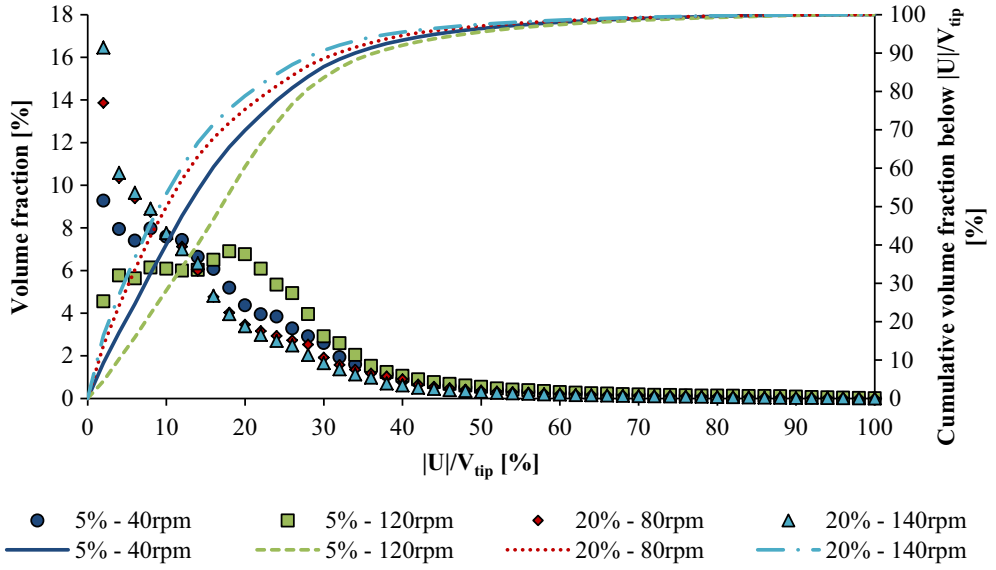

Fig. 21. Volume fraction of total fluid moving at different fractions of relative tip speed and cumulative volume fraction of fluid moving at velocities below $|\mathbf{U}|/\mathbf{V}_{tip}$. The phase angle of the impeller is the same as in Fig. 20.

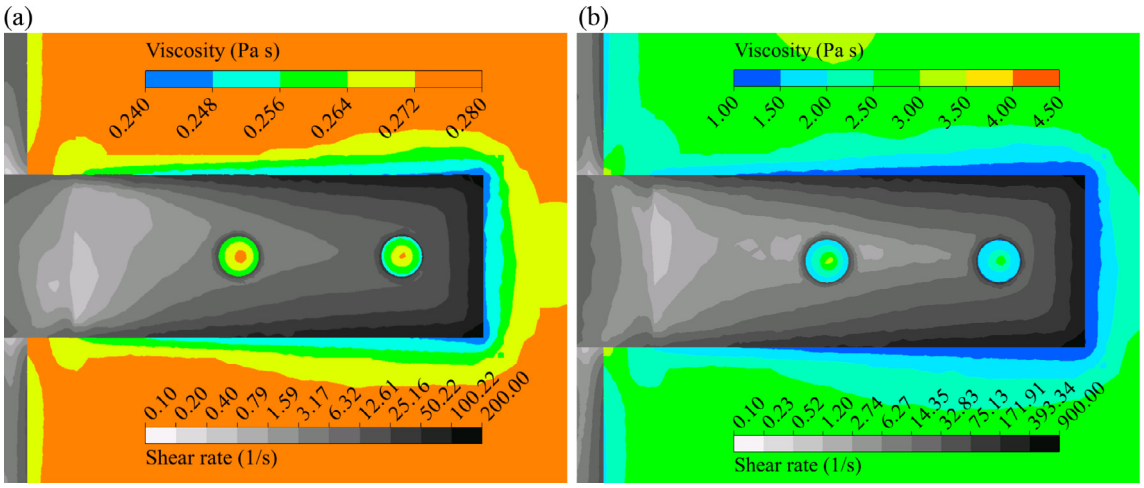

Fig. 22. Shear rate profiles on the top right blade and viscosity profiles in the adjacent fluid (a) 5% gel and 40 rpm, (b) 20% gel and 140 rpm.

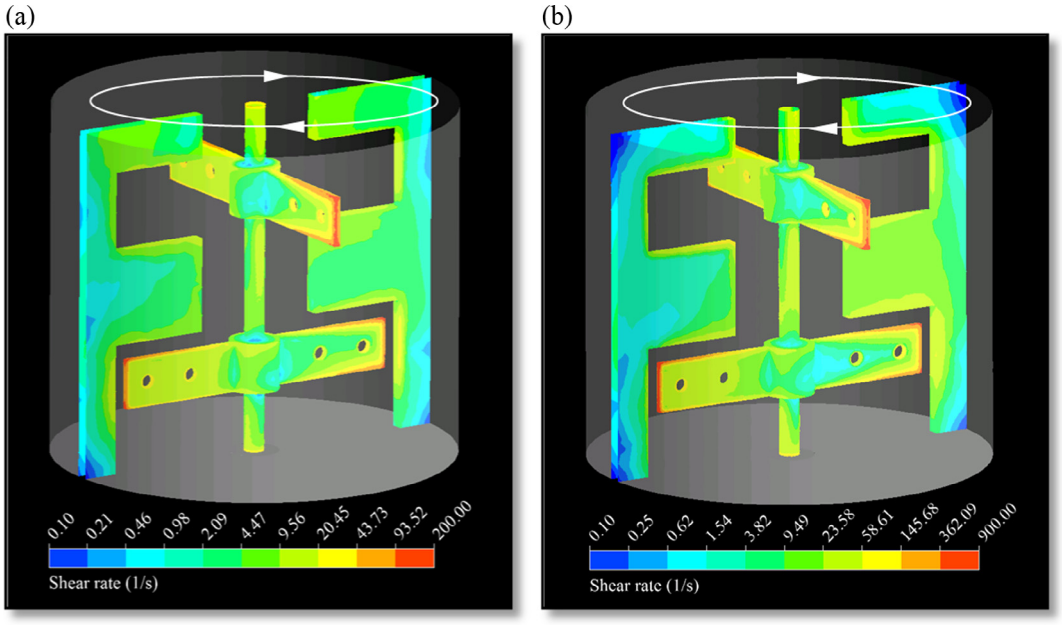

Fig. 23. Shear rate profiles in the impeller and the baffles (a) 5% gel and 40 rpm, (b) 20% gel and 140 rpm.

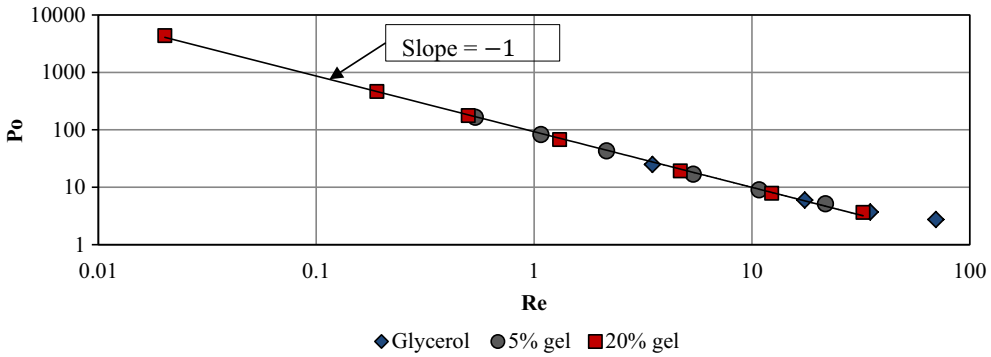

Fig. 24. Power curves of the mixing system with the two mixtures (20% and 5%wt gel) and with glycerol.

3.4. Power consumption

To better characterize the impeller behaviour, we investigated the power required to mix both Newtonian and non-Newtonian fluids at different operating conditions. Since the PIV validation of the CFD model has given a positive outcome, we have confidence in the accuracy of the model and therefore we now use it to predict power consumption. To do so, we computed the torque on the impeller surface at each impeller position over an entire revolution, and we average it to calculate the power consumption of the impeller. The details of how to calculate the power consumption of the impeller from the computed torque can be found elsewhere (Cortada-Garcia et al., 2017). The results are presented in Fig. 24. To construct the power curves, we followed the Metzner and Otto approach (Metzner and Otto, 1957) as presented in Section 3.1, and we used Eq. (3) to compute the value of the Reynolds number. As previously mentioned, the constant of our impeller is 15.

As can be seen in Fig. 24, the laminar regime, where the power curve has a slope of −1 in a double logarithmic plot of the Power number against the Reynolds number, extends up to Re approximately equal to 50. Our experiments also include the early transition regime as shown in Section 3.1, and the CFD simulations predict adequately the flow behaviour in both flow regimes.

The Metzner and Otto constant can be used to compare the efficiency of the impeller with that of other impellers used to mix non-Newtonian fluids. The lower the value of this constant, the less the power required by the impeller to agitate the fluid at a given Reynolds number. The impeller that we studied has a similar performance to Maxblend™, which is extensively used in industrial applications related to the mixing of highly viscous fluids. The Maxblend™ constant is in the range of 15–20 (Stobiac et al., 2014, Patel et al., 2011, Fradette et al., 2007). The Paravisc™ impeller is also used in industrial applications dealing with highly viscous fluids, and its constant is significantly higher; it is approximately 30 (Iranshahi et al., 2006). Other common configurations for mixing of highly viscous non-Newtonian fluids are two coaxial impellers, a central one, such as the Scabba impeller or the Rushton turbine, and an external one, such as an anchor impeller. The Scabba impeller and the Rushton turbine have similar constants: 10.5 (Pakzad et al., 2013b) and 9.6–11.5 (Cortada-Garcia et al., 2017, Patel et al., 2012), respectively. In contrast, anchor impellers have larger constants of around 23 (Pakzad et al., 2013a). Different methodologies have been proposed to obtain power curves for coaxial mixers (Thibault and Tanguy, 2002, Foucault et al., 2004, Farhat et al., 2008, Pakzad et al., 2013a), but direct comparison of power consumption between single and coaxial impellers has not been reported in the literature.

Although impellers with low constant are desirable, the design of the mixing tank cannot be based only on this coefficient. For instance, the agitation of highly viscous shear thinning fluids and yield stress fluids with impellers such as the Rushton turbine or the Scabba impeller leads to pseudo-cavern and cavern formation, respectively. In contrast, the impeller presented in this study has a higher constant, but, as shown in Section 3, it minimises stagnant zones, so it is preferable in this case.

4. Conclusions

In this study, we have characterized computationally the flow behaviour of shear thinning fluids (modeled with the Carreau law) in a scaled-down mixing tank used in the manufacturing of complex oral health products. We have validated the CFD model against experimental velocity profiles obtained with PIV. The experimental errors were thoroughly assessed and presented in the form of error bars. We identified the interrogation error to be the most significant in our case. The maximum uncertainty when comparing the computational and experimental results was also evaluated. Overall, experiments and simulations agree quite well. The impeller performance was assessed both qualitatively and quantitatively. We first reported velocity streamlines; these revealed that the impeller generates strong transverse motion compared with the axial and radial components. Then we identified the regions in which the fluid is agitated more vigorously (with higher velocity), and we were able to quantify the percentage of the fluid that has speeds above given thresholds. We concluded with this study that the impeller is capable of minimizing stagnant zones, but most of the fluid has a velocity ten times smaller than that of the tip of the blade. This situation is worsened for fluids with higher viscosity and higher shear thinning behaviour (that of 20% gel). We also evaluated the effect of the holes in the fluid flow, and we concluded that they increase the shear rate locally by increasing the perimeter of the edges of the impeller. This result is positive for shear thinning fluids, since the viscosity is reduced locally, but it can be counter-productive for shear thickening fluids. Power curves were calculated from the CFD results, which showed that the Metzner and Otto constant for this impeller is comparable to other industrial impellers used for viscous liquids. This study intended to demonstrate the importance of performing careful studies when designing mixers to deal with complex fluids.

Acknowledgements

The authors would like to acknowledge GlaxoSmithKline Consumer Healthcare and EPSRC for the financial support given to this project.

References

Adrian, R.J., Westerweel, J., 2011. Particle Image Velocimetry. Cambridge University Press.
Arratia, P.E., Kukura, J., Lacombe, J., Muzzio, F.J., 2006. Mixing of shear-thinning fluids with yield stress in stirred tanks. AICHE J. 52, 2310–2322.
Baldi, S., Yianneskis, M., 2004. On the quantification of energy dissipation in the impeller stream of a stirred vessel from fluctuating velocity gradient measurements. Chem. Eng. Sci. 59, 2659–2671.
Cortada-Garcia, M., Dore, V., Mazzei, L., Angeli, P., 2017. Experimental and CFD studies of power consumption in the agitation of highly viscous shear thinning fluids. Chem. Eng. Res. Des. 119, 171–182.
Couerbe, G., Fletcher, D.F., Xuereb, C., Poux, M., 2008. Impact of thixotropy on flow patterns induced in a stirred tank: numerical and experimental studies. Chem. Eng. Res. Des. 86, 545–553.
Coussot, P., Nguyen, Q.D., Huynh, H.T., Bonn, D., 2002. Avalanche behavior in yield stress fluids. Phys. Rev. Lett. 88.
de Graef, V., Depypere, F., Minnaert, M., Dewettinck, K., 2011. Chocolate yield stress as measured by oscillatory rheology. Food Res. Int. 44, 2660–2665.
Delafosse, A., Line, A., Morchain, J., Guiraud, P., 2008. LES and URANS simulations of hydrodynamics in mixing tank: comparison to PIV experiments. Chem. Eng. Res. Des. 86, 1322–1330.
Farhat, M., Fradette, L., Tanguy, P.A., 2008. Revisiting the performance of a coaxial mixer. Indust. Eng. Chem. Res. 47, 3562–3567.
Fontaine, A., Guntzburger, Y., Bertrand, F., Fradette, L., Heuzey, M.C., 2013. Experimental investigation of the flow dynamics of rheologically complex fluids in a Maxblend impeller system using PIV. Chem. Eng. Res. Des. 91, 7–17.
Foucault, S., Ascanio, G., Tanguy, P.A., 2004. Coaxial mixer hydrodynamics with Newtonian and non-Newtonian fluids. Chem. Eng. Technol. 27, 324–329.
Fradette, L., Thome, G., Tanguy, P.A., Takenaka, K., 2007. Power and mixing time study involving a Maxblend (R) impeller with viscous Newtonian and non-Newtonian fluids. Chem. Eng. Res. Des. 85, 1514–1523.
Gabriele, A., Nienow, A.W., Simmons, M.J.H., 2009. Use of angle resolved PIV to estimate local specific energy dissipation rates for up- and down-pumping pitched blade agitators in a stirred tank (vol 64, pg 126, 2009). Chem. Eng. Sci. 64. 4196-4196.
Green, D.W., 2008. Perry's Chemical Engineers' Handbook. McGraw-Hill, New York, pp. 48–49. Section 8.
Guntzburger, Y., Fontaine, A., Fradette, L., Bertrand, F., 2013. An experimental method to evaluate global pumping in a mixing system: application to the Maxblend (TM) for Newtonian and non-Newtonian fluids. Chem. Eng. J. 214, 394–406.

Hiruta, O., Yamamura, K., Takebe, H., Futamura, T., Iinuma, K., Tanaka, H., 1997. Application of maxblend fermentor(R) for microbial processes. J. Fermentation Bioeng. 83, 79–86.
Iranshahi, A., Heniche, M., Bertrand, F., Tanguy, P.A., 2006. Numerical investigation of the mixing efficiency of the Ekato Paravisc impeller. Chem. Eng. Sci. 61, 2609–2617.
Kazemzadeh, A., Ein-Mozaffari, F., Lohi, A., Pakzad, L., 2016. Effect of the rheological properties on the mixing of Herschel-Bulkley fluids with coaxial mixers: applications of tomography, CFD, and response surface methodology. Can. J. Chem. Eng. 9999, 1–13.
Kresta, S.M., Etchells III, A.W., Dickey, D.S., Atiemo-Obeng, V.A., 2015. Advances in Industrial Mixing.
Mavros, P., 2001. Flow visualization in stirred vessels – a review of experimental techniques. Chem. Eng. Res. Des. 79, 113–127.
Metzner, A., Otto, R., 1957. Agitation of non-Newtonian fluids. AIChE J. 3, 3–10.
Moffat, R.J., 1988. Describing the uncertainties in experimental results. Exp. Therm. Fluid Sci. 1, 3–17.
Montante, G., Bakker, A., Paglianti, A., Magelli, F., 2006. Effect of the shaft eccentricity on the hydrodynamics of unbaffled stirred tanks. Chem. Eng. Sci. 61, 2807–2814.
Pakzad, L., Ein-Mozaffari, F., Upreti, S.R., Lohi, A., 2013a. Agitation of Herschel-Bulkley fluids with the Scaba-anchor coaxial mixers. Chem. Eng. Res. Des. 91, 761–777.
Pakzad, L., Ein-Mozaffari, F., Upreti, S.R., Lohi, A., 2013b. Characterisation of the mixing of non-newtonian fluids with a scaba 6SRGT impeller through ert and CFD. Can. J. Chem. Eng. 91, 90–100.
Patel, D., Ein-Mozaffari, F., Mehrvar, M., 2011. Dynamic performance of continuous-flow mixing of pseudoplastic fluids exhibiting yield stress in stirred reactors. Indust. Eng. Chem. Res. 50, 9377–9389.
Patel, D., Ein-Mozaffari, F., Mehrvar, M., 2012. Improving the dynamic performance of continuous-flow mixing of pseudoplastic fluids possessing yield stress using Maxblend impeller. Chem. Eng. Res. Des. 90, 514–523.
Patel, D., Ein-Mozaffari, F., Mehrvar, M., 2015. Effect of rheological parameters on non-ideal flows in the continuous-flow mixing of biopolymer solutions. Chem. Eng. Res. Des. 100, 126–134.
Ramsay, J., Simmons, M.J.H., Ingram, A., Stitt, E.H., 2016. Mixing of Newtonian and viscoelastic fluids using "butterfly" impellers. Chem. Eng. Sci. 139, 125–141.
Schramm, G., 1994. A Practical Approach to Rheology and Rheometry, Haake Karlsruhe.
Sharp, K.V., Adrian, R.J., 2001. PIV study of small-scale flow structure around a Rushton turbine. Aiche J. 47, 766–778.
Sossa-Echeverria, J., Taghipour, F., 2015. Computational simulation of mixing flow of shear thinning non-Newtonian fluids with various impellers in a stirred tank. Chem. Eng. Process.: Process Intensification 93, 66–78.
Stobiac, V., Fradette, L., Tanguy, P.A., Bertrand, F., 2014. Pumping characterisation of the maxblend impeller for Newtonian and strongly non-newtonian fluids. Can. J. Chem. Eng. 92, 729–741.
Sumitomo, 2017. MAXBLEND [Online]. Sumitomo Heavy Industries Process Equipment. Available: <http://www.shi-pe.shi.co.jp/english/products/mixing/maxblendclub/mbabout/> 2017].
Thibault, F., Tanguy, P.A., 2002. Power-draw analysis of a coaxial mixer with Newtonian and non-Newtonian fluids in the laminar regime. Chem. Eng. Sci. 57, 3861–3872.
Westerlins, 2016. Butterfly dissolvers [Online]. Sweden: Westerlins Maskinfabrik AB Available: <http://www.westerlins.com/products/butterfly-dissolvers/>.
Westerweel, J., Scarano, F., 2005. Universal outlier detection for PIV data. Exp. Fluids 39, 1096–1100.
Zadghaffari, R., Moghaddas, J.S., Revstedt, J., 2009. A mixing study in a double-Rushton stirred tank. Comput. Chem. Eng. 33, 1240–1246.
Zhu, H., Kim, Y., de Kee, D., 2005. Non-Newtonian fluids with a yield stress. J. Non-Newtonian Fluid Mech. 129, 177–181.